Advances in critical temperature shift modeling of confined pure fluids using the Kihara potential function

Mohammad Humand[1] · Mohammad Reza Khorsand Movaghar[1] · Mobarakeh Mohammadpour[1] · Guillermo J. Zarragoicoechea[2] · Mostafa Abbaszadeh[3]

Abstract
A multitude of research works have been conducted in the past decade to better predict the change of critical properties of fluids confined in nanopores, known as critical shift, due to its great impact upon calculations of fluid properties in tight reservoirs. Modeling of this phenomenon commenced with developing equations of state (EOS) and has been continuing with correlations, all based on the two-parameter Lennard–Jones (L–J) potential function. Although these approaches have tried to present passable estimations of critical shift, sufficiently accurate predictions of critical shift are still missing in the literature. In this study, the three-parameter Kihara potential, as a more physically realistic alternative, is used to develop the van der Waal (vdW) EOS, and accordingly, a fluid-dependent expression is derived to calculate the critical temperature of confined fluids, i.e., pore critical temperature (T_{cp}). Using 50 data points of T_{cp} reports for normal alkanes in the literature, the average error of our model is only 2.23%, 6.4% less than that of the L–J model. Furthermore, despite simple correlations of previous works, herein the Kihara parameters are exclusively tuned for each component based on their T_{cp} reports, which resulted in an average error of 0.4% for normal alkanes. Finally, the pressure–volume diagrams of vdW and Peng–Robinson EOSs associated with the Kihara potential function are comprehensively discussed. The findings of this study can help researchers with more accurate predictions of the critical temperature of fluids confined in tight porous media, thereby providing more precise calculations of fluid properties and behavior at equilibrium conditions.

Keywords Confined fluids · Kihara potential · Phase transition · Critical shift · Nanopores

Abbreviations

AARD	Average Absolute Relative Deviation
EOS	Equation of State
L-J	Lennard–Jones
P-V	Pressure–Volume
PR	Peng–Robinson
vdW	Van der Waals
VLE	Vapor-Liquid Equilibrium

List of Symbols

a_k	Kihara spherical core radius (Å or m in Eq. 4)
a_k^*	Reduced Kihara parameter (-)
a_{PR}	Peng–Robinson constant
a_{vdW}	Van der Waals constant ($m^3.Pa.mol^{-2}$)
A	Transverse pore reduced area (–)
b_{PR}	Peng–Robinson constant
b_{vdW}	Van der Waals constant ($m^3.mol^{-1}$)
C	Coefficients (–)
f(T)	Free energy of ideal gas (J)
F	Helmholtz free energy (J)
G	Gibbs free energy (J)
k	Boltzmann constant ($J.K^{-1}$)
L	Length (m)
MW	Molecular weight ($Kg.Kgmol^{-1}$)
N	System particles (-)
P	System pressure (Pa)
P_c	Bulk critical pressure (MPa)
P_{cp}	Pore critical pressure (*MPa*)
r	Distance between molecular centers (m)
r_p	Pore size (nm)

✉ Mohammad Reza Khorsand Movaghar
m.khorsand@aut.ac.ir

[1] Department of Petroleum Engineering, Amirkabir University of Technology, No. 424, Hafez Ave, Tehran 15914, Iran

[2] IFLYSIB (UNLP, CONICET), Universidad Nacional de La Plata, Comisión de Investigaciones Científicas de La Prov. de Buenos Aires, 1900 La Plata, Argentina

[3] Department of Applied Mathematics, Faculty of Mathematics and Computer Science, Amirkabir University of Technology, No. 424, Hafez Ave, Tehran 15914, Iran

S	Entropy (J.K^{-1})
T	System temperature (K)
T^*	Reduced temperature (–)
T_c	Bulk critical temperature (K)
T_{ch}	Hysteresis critical temperature (K)
T_{cp}	Pore critical temperature (K)
T_r	Bulk reduced temperature (–)
U	Internal energy (J)
$U(r_{12})$	Potential function
v	Molar volume (m^3.mol^{-1})
V	System volume (m^3)
z_c	Critical compressibility factor (–)

Greek letters

β	$1/kT\left(J^{-1}\right)$
δ_p	Adsorption thickness (nm)
ε	Kihara energy parameter (J)
ε_k	$\varepsilon/k(K)$
σ_k	Kihara size parameter (Å or m in Eq. 4)
σ_{LJ}	Lennard–Jones size parameter (Å)
ω	Acentric factor (–)

Introduction

In recent years, myriads of efforts have been made to understand and evaluate the phase behavior of fluids confined in molecular-scale media, especially hydrocarbons mainly because of the growing demand for production from unconventional reserves, such as shale oil and tight gas. The phenomenon of changes in the critical properties of matters due to confinement is originally known as critical shift and even its applicability has been investigated in several other research areas, such as nanofluidic chipset technologies (Alfi et al. 2016).

Phase behavior and thermodynamics of confined fluids have a significant deviation from their corresponding bulk behavior. Experimental measurements (Morishige and Ito 2002; Morishige and Shikimi 1998; Morishige et al. 2003; Tan et al. 2019) have shown that the thermodynamic and physicochemical properties of fluids, such as critical properties, substantially shift when they are confined in a porous medium with nanometric pore radius. Hence, incorporating the bulk properties (not confined state) of matters in phase behavior calculations undoubtedly leads to poor results.

Various analytical and numerical methods have been examined to predict and model the mentioned theory for pure fluids, e.g., the developed van der Waals (vdW) equation of state (EOS) in the previous study (Zarragoicoechea and Kuz 2002), extended Peng–Robinson and Soave–Redlich–Kwong EOSs (Islam and Sun 2017; Zhang et al. 2019a, b), density functional theory (Evans et al. 1986), and Monte Carlo simulations (Jiang et al. 2004; Jin and Nasrabadi 2016; Lowry

and Piri 2018; Singh et al. 2009). Numerical approaches are frequently inconvenient to be applied to a different study scope since they are accompanied by numerous limitations. Having a theoretical and thermodynamic basis, the modified vdW EOS developed by Zarragoicoechea and Kuz has been widely used because of its compatibility with experimental values on the one hand, and its ease of use on the other. Such a convenience would be much preferable to implementing time-consuming and inconvenient huge numerical and molecular simulations for every research case. The EOS approach was developed based on the Lennard–Jones (L–J) potential function with two adjustable parameters (σ_{LJ}, ε/k) whose values can be determined via least-square data analysis of thermodynamic properties, such as experimental reports of viscosity or second virial coefficient (Tee et al. 1966a, b). A three-parameter potential function, nevertheless, is expected to provide more accurate modeling due to its flexibility and more realistic physics.

On the other hand, fluid adsorptions and their huge impacts on phase behavior could have not been ignored (Zhang et al. 2018a, b, c; Zhang et al. 2019a, b). A multi-layer film of fluid is always adsorbed to the pore walls and its contribution to the confined fluid characteristics is great enough to be considered, because in nanoscale (confined) porous media, the wall-molecule interactions are not insignificant anymore as they are in the bulk state. In this regard, analytical (Wang et al. 2021; Zhang et al. 2018a, b, c; Zhang et al. 2019a, b) and numerical (Jiang et al. 2005; Peng et al. 2007; Tan et al. 2017; Wong, et al. 2009) research works have been conducted to include the adsorption phenomenon. Although experimental measurements are always highly reliable and give direct understanding of fluid properties, they are greatly time-consuming and highly expensive setups are needed for confined porous media to be studied. Moreover, it is quite difficult to establish an apparatus that could last under extreme conditions of high pressure and temperature (Zhang et al. 2019a, b).

Over the last few years, various measures have been taken in order to enhance the confinement modeling of pure fluids, though no fundamental and analytical development was presented except the previous original model of L–J (Zarragoicoechea and Kuz 2002). Other fellow researchers have manipulated numbers and coefficients through curve fitting to merely modify every possible aspect of the basic model (Jin et al. 2013; Song et al. 2020; Yang et al. 2019; Yang and Li 2020). In several works, moreover, the mentioned L–J approach has just been repeated with corrections of the theory's coefficients (Islam et al. 2015; Zhang et al. 2018a, b, c; Zhang et al. 2018a, b, c). These numerical enhancements are strongly related to the available data sets of one specific fluid, and possibly not appropriate for comprehensive applications. Such uncertainty even led to developing exclusively

curve-fitted correlations for specific substances, e.g., methane, ethane and carbon dioxide (Tan et al. 2019; Yang et al. 2019).

Kihara potential, despite the Lennard–Jones, is a three-parameter potential function that incorporates the hard-impenetrable core of a molecule into the modeling by its third parameter a_k (Kihara 1953). In the L–J model, however, there is no limitation for two approaching molecules and they can completely interpenetrate. Kihara successfully fits thermodynamic data, specifically the second virial coefficient, for various types of fluids. L–J potential, in contrast, performs weaker in lower temperatures, and the flexibility of Kihara potential makes it much easier to have a perfect fitting (Prausnitz et al. 1998).

In the current work, first, the Kihara potential function is employed to develop the energy integral and derive the vdW-EOS with which the hysteresis critical temperature (T_{ch}) of confined fluids including argon, nitrogen, oxygen, carbon dioxide, ethylene, and xenon is calculated. Second, the Kihara parameters are adjusted with a brand-new and concrete adjustment method on a thermodynamic basis to achieve compatibility with bulk critical properties. Accordingly, the pore critical temperature (T_{cp}) is calculated for some components comprising nitrogen, carbon dioxide, methane, ethane, propane, n-butane, and n-octane with substantial error reduction. Third, the Kihara parameters are tuned based on the reported T_{cp} empirical reports to have the most likely precise predictions. Finally, the Peng–Robinson (PR) EOS is developed to evaluate and discuss the pressure–volume (P–V) diagrams of fluids confined in nanopores with respect to reduction in pore size. In general, 80 data points are examined to evaluate the capabilities of the proposed model, which is one of the most significant collections of critical temperature shift points ever gathered from research articles (Jiang et al. 2004; Jin and Nasrabadi 2016; Lowry and Piri 2018; Morishige and Shikimi 1998; Morishige et al. 2003; Pitakbunkate et al. 2016; Singh et al. 2009; Tan et al. 2019). Previous studies (Jin et al. 2013; Song et al. 2020; Yang et al. 2019; Yang and Li 2020), however, employed much fewer data points for developing their model, among which Yang and Li (2020) had the largest number of data points, i.e., 53. It is noteworthy that the data used in their work belonged, to a large extent, to methane and the diversity of studied fluids was not wide at all.

This study will address the following major research gaps:

- Developing the vdW EOS for confined fluids using a more physically realistic potential function
- Presenting a fluid-dependent expression for critical temperature shift modeling
- Applying a thermodynamic-based adjustment method to acquire a more accurate method to calculate pore critical temperature

Model and theory

At the first step, the conventional vdW EOS must be developed in a modified form to describe the confinement phenomenon. Although this EOS is a simple, it has the qualities and abilities to properly predict the critical and vapor–liquid equilibrium (VLE) properties, i.e., the properties of matters in liquid and gaseous phases at equilibrium. As shown in Fig. 1, we consider a Cartesian pore model consisting of confined particles interacting through any pair potential. For this model, the pressure $\vec{P}$ [Pa] is a diagonal tensor with components $\vec{P}(p_i, i = x, y, z)$. We start with the Gibbs free energy (G) [J] of the fluids which is given by (Smith et al. 2005),

$$G(p, T) = U + P_i V - TS \tag{1}$$

where U is the internal energy [J]; P is the system pressure [Pa]; T is the system temperature [K]; V is volume of the system [m³]; and S is the entropy [J.K⁻¹]. Besides, the equation for internal energy is as follows (Borgnakke and Sonntag 2012),

$$dU = TdS - P_i dV \tag{2}$$

The pressure expression of vdW EOS can be derived using the derivate of Helmholtz free energy with respect to volume. The Helmholtz free energy of a system including N particles interacting by a pair potential $U(r_{12})$ can be derived from the perturbation theory as (Hansen and McDonald 1990)

$$F = f(T) - \frac{kTN^2}{2V^2} \iint \left(e^{-\beta U(r_{12})} - 1 \right) dV_1 dV_2 \tag{3}$$

where f(T) is the free energy of ideal gas [J]; k is the Boltzmann constant [J.K⁻¹]; and β is $1/kT$ [J⁻¹]. The term $e^{-\beta U(r_{12})} - 1$ is often called the Mayer function. Here, in spite of the former work (Zarragoicoechea and Kuz 2002), we utilized the Kihara potential (Fig. 2) for the interactions
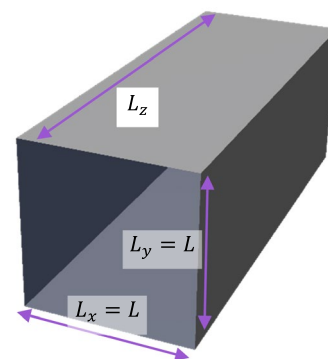

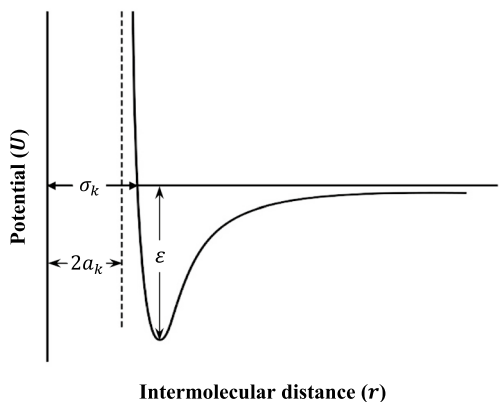**Fig. 1** Schematic of a nano-scale pore in Cartesian coordinates

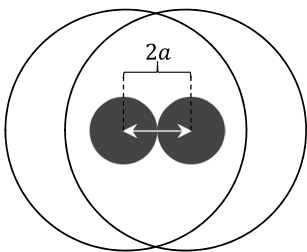**Fig. 2** Kihara potential function with three adjustable parameters

Fig. 3 A specific position of two molecules in which the value of the Kihara potential function approaches to infinity

between particles. In the Lennard–Jones theory, two molecules can completely interpenetrate provided that they have enough energy (Prausnitz et al. 1998), whereas according to the Kihara model, the repulsion interaction in the rigid spherical core is split into two parts; a rigid core and an outer soft spherical repulsion region (Reed and Gubbins 1973). Therefore, as Fig. 3 shows, we suppose that soft-penetrable electron clouds surround a hard-impenetrable core whose mathematical expression would be as (Prausnitz et al. 1998),

$$
U(r_{12}) = \begin{cases} \infty & r < 2a_k \\ 4\varepsilon\left[\left(\frac{\sigma_k - 2a_k}{r - 2a_k}\right)^{12} - \left(\frac{\sigma_k - 2a_k}{r - 2a_k}\right)^6\right] & r \geq 2a_k \end{cases} \quad (4)
$$

where a_k is the radius of the spherical core [m]; ε [J] is the depth of the energy well (we employ $\varepsilon_k = \varepsilon/k$ [K] as the third Kihara parameter instead of ε in this study); and σ_k is the collision diameter [m], i.e., the distance r [m] between molecular centers when $U(r_{12}) = 0$. The intermolecular distance goes from $r_{12} = 2a_k$ (where the repulsion force is infinity) to $r_{12} = \infty$.

Given the Eq. (3), the standard vdW equation can be derived by integrating over an infinite volume. For a finite volume, the same procedure can be applied by splitting the integral into two regions, $2a_k < r_{12} < \sigma_k$ and $r_{12} > \sigma_k$:

$$
F = f(T) - \frac{kTN^2}{2V^2}
$$
$$
\left[\iint\limits_{2a<r_{12}<\sigma} \left(e^{-\beta U(r_{12})} - 1\right)dV_1 dV_2 + \iint\limits_{r_{12}>\sigma} \left(e^{-\beta U(r_{12})} - 1\right)dV_1 dV_2\right] \quad (5)
$$

Assuming two approximations for each integral, $e^{-\beta U(r_{12})} \cong 0$ for the former because $U(r_{12}) \to \infty$ and $e^{-\beta U(r_{12})} \cong 1 - U(r_{12})/kT$ for the latter, Eq. (5) becomes

$$
F = f(T) + \frac{kTN^2}{V}b + \frac{kTN^2}{2V^2}\iint\limits_{r_{12}>\sigma} \frac{U(r_{12})}{kT}dV_1 dV_2 \quad (6)
$$

with $b = \frac{2\pi}{3}\left(\sigma_k^3 - (2a_k)^3\right)$ and $V = L_x L_y L_z$ in which $L_x = L_y = L$ and $L_z = L_z$ for a pore model in the Cartesian coordinates.

The expression for b – that is slightly different between the Kihara and L-J potentials – comes from the analytical solution of the first integral in Eq. (5). Since b represents the repulsive term, its form clearly manifests the effect of the hard-core during the repulsion. The integral in Eq. (6) can be semi-analytically calculated as,

$$
\frac{1}{V}\iint\limits_{r_{12}>\sigma} \frac{U(r_{12})}{kT}dV_1 dV_2 = \frac{4\varepsilon}{kT}\sigma_k^3 I(A, a_k^*) \quad (7)
$$

$$
I(A, a_k^*) = C_0(a_k^*) + \frac{C_1(a_k^*)}{\sqrt{A}} + \frac{C_2(a_k^*)}{A} \quad (8)
$$

where $A = L_x L_y/\sigma_k^2$ is the reduced area of the square cross section of a pore, a_k^* is the reduced Kihara parameter $(2a_k/\sigma_k)$, and C_0 to C_2 are coefficients obtained from the numerical integration. Yet, C_0. has an analytical expression (Eq. (9)) that is achieved from the integral when $A = \infty$. Besides, C_1 and C_2 can be obtained from nonlinear fitting for each fluid that will be presented in Sect. "Results and discussion".

$$
C_0(a_k^*) = \frac{2\pi}{495}(a_k^* - 1)(220 + a_k^*(31a_k^* - 143)) \quad (9)
$$

The Helmholtz free energy of a confined fluid is formulated by Eq. (10) derived through applying the ideal gas free energy $(f(T) = -NkT[\ln V/N + c]$ (Hill 1986)), writing $C_0 = -a_k/2\varepsilon\sigma_k^3$, and considering the limited compressibility of matter via the substitution $\ln V - \left(\frac{N}{V}\right)b \sim \ln(V - Nb)$.

$$F = f(T) - \mathrm{NkTln}(V - Nb)$$
$$+ 2\frac{N^2}{V}\varepsilon\sigma_k^3\left(-\frac{a_k}{2\varepsilon\sigma_k^3} + \frac{C_1(a_k^*)}{\sqrt{A}} + \frac{C_2(a_k^*)}{A}\right) \quad (10)$$

In the vdW theory, a molecule's volume (volume excluded from the system) is represented by variable b that is, in other words, the available space for molecules to overlap. With this definition, other molecules will have an accessible volume of $V - Nb$ to move in (Johnston 2014). This is the backbone of the idea laying behind the substitution for Eq. (10) which is concretely independent of the applied potential function.

As shown in Fig. 1, a cross section confinement occurs in an axially infinite pore for which the axial (P_{zz}) and transverse (P_{xx} and P_{yy}) components of the pressure tensor $\vec{P}$ are as follows,

$$P_{xx} = P_{yy} = -\frac{\sigma_k^2}{A}\frac{\partial F}{\partial L} \quad (11)$$

$$P_{zz} = -\frac{\sigma_k^2}{A}\frac{\partial F}{\partial A} \quad (12)$$

Using Eqs. (11) and (12), and applying Eq. (10), the axial and transverse components are given by Eq. (13) and (14).

$$P_{xx} = P_{yy} = \frac{\mathrm{NkT}}{V - Nb} - \frac{N^2}{V^2}\left[a - \varepsilon\sigma_k^3\left(3\frac{C_1(a_k^*)}{\sqrt{A}} + 4\frac{C_2(a_k^*)}{A}\right)\right] \quad (13)$$

$$P_{zz} = \frac{\mathrm{NkT}}{V - Nb} - \frac{N^2}{V^2}\left[a - 2\varepsilon\sigma_k^3\left(\frac{C_1(a_k^*)}{\sqrt{A}} + \frac{C_2(a_k^*)}{A}\right)\right] \quad (14)$$

Clearly, when $A \to \infty$, the bulk vdW equation is obtained and $P_{xx} = P_{yy} = P_{zz}$. In reduced coordinates, Eqs. (13) and (14) can be written as,

$$P_{xx}^* = P_{yy}^* = \frac{T^*}{v^* - b^*} - \frac{a^* - \left(3\frac{C_1(a_k^*)}{\sqrt{A}} + 4\frac{C_2(a_k^*)}{A}\right)}{v^{*2}}, \quad (15)$$

$$P_{zz}^* = \frac{T^*}{v^* - b^*} - \frac{a^* - 2\left(\frac{C_1(a_k^*)}{\sqrt{A}} + \frac{C_2(a_k^*)}{A}\right)}{v^{*2}}, \quad (16)$$

where $P^* = P\sigma_k^3/\varepsilon$; $T^* = \mathrm{k}T/\varepsilon$; $v^* = (V/N)\sigma_k^{-3}$; $b^* = b\sigma_k^{-3}$; and $a^* = a/\varepsilon\sigma_k^3$.

From the theory of corresponding states and the continuity principle of gaseous and liquid phases, the following conditions are required for vdW type EOSs at the critical point (Danesh 1998):

$$\left(\frac{\partial P_{zz}^*}{\partial v^*}\right)_{T^*=T_c^*} = \left(\frac{\partial^2 P_{zz}^*}{\partial v^{*2}}\right)_{T^*=T_c^*} = 0 \quad (17)$$

Applying the requirements, we are furnished with the critical properties' equations.

$$T_c^* = \frac{8}{27b^*}\left(a^* - 2\frac{C_1(a_k^*)}{\sqrt{A}} - 2\frac{C_2(a_k^*)}{A}\right) \quad (18)$$

$$P_c^* = \frac{a^* - 2\frac{C_1(a_k^*)}{\sqrt{A}} - 2\frac{C_2(a_k^*)}{A}}{27b^{*2}} \quad (19)$$

$$v_c^* = 3b^* \quad (20)$$

Correspondingly, the above modeling can be applied to nano-scale pores in cylindrical coordinates (Fig. 4) in which pores are infinite over the Z direction. This is what has been considered for all calculations in this work, similar to the previous work (Zarragoicoechea and Kuz 2002) in which the square section area in Eq. (18) is equated to the area corresponding to the experimental cylindrical pore, $A = \pi(r_p/\sigma_k)^2$. Equations (18) and (19) reveal a shift in the critical temperature and pressure in comparison with those of the bulk vdW equation.

Since molecule-wall interactions always lead to forming of a layer onto the pore walls (adsorption thickness, δ_p [nm]), the available volume for free fluid molecules to move will shrink. To consider adsorption thickness in our modelling, we use some measured data for various fluids from the literature, i.e., adsorption thickness at different pore sizes. Since these reported adsorption thicknesses are not necessarily measured at our desired pore radii, we attempt to find a correlation, exclusively for each component, that would have the least possible deviation from the measured data.
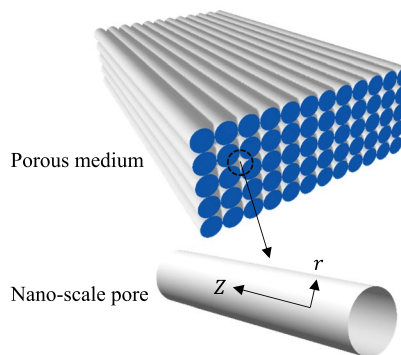

Fig. 4 Schematic of a nano-scale pore in cylindrical coordinates

Mathematically, there will be a slight change in Eq. (18) and the areal cross section would decrease due to the adsorption thickness. Therefore, the critical temperature and pressure shift equations turn into:

$$T_c^* = \frac{8}{27b^*}\left(a^* - 2\frac{C_1\left(a_k^*\right)}{\sqrt{\pi}\left(\frac{r_p - \delta_p}{\sigma_k}\right)} - 2\frac{C_2\left(a_k^*\right)}{\pi\left(\frac{r_p - \delta_p}{\sigma_k}\right)^2}\right) \tag{21}$$

$$P_c^* = \frac{a^* - 2\frac{C_1\left(a_k^*\right)}{\sqrt{\pi}\left(\frac{r_p - \delta_p}{\sigma_k}\right)} - 2\frac{C_2\left(a_k^*\right)}{\pi\left(\frac{r_p - \delta_p}{\sigma_k}\right)^2}}{27b^{*2}} \tag{22}$$

where δ_p [nm] is the adsorption thickness for which here we employ the values Zhang et al. (2019a; b) have reported in their work. In this study, instead of a logarithmic function proposed in their paper, a rational model as Eq. (23) is used for least square fitting that results in less deviation:

$$\delta_p = \frac{a + b \times r_p}{1 + c \times r_p + d \times r_p^2} \tag{23}$$

in which r_p and δ_p are both in nm. Moreover, a, b, c, and d are coefficients whose values are listed in Table 1 for N_2, CO_2, and normal alkanes from CH_4 to n-$C_{10}H_{22}$. Figure 5 shows the measured (Zhang et al. 2019a, b) and fitted values of δ_p. Clearly, there is a decreasing trend as pore radius increases, implying that the effect of adsorption thickness is less at larger pores.

Furthermore, the following expressions may be used for normal alkanes based on the values presented in Table 1:

$$a = 0.12\ln\omega + 1.0495 \quad R^2 = 0.9235 \tag{24}$$

$$b = 0.0225\ln\omega + 0.1332 \quad R^2 = 0.8675 \tag{25}$$

$$c = -1.0654\omega^2 + 0.1643\omega + 0.6555 \quad R^2 = 0.7315 \tag{26}$$

$$d = 6.3464 \times 10^{-6}\ln\omega - 5.9508 \times 10^{-6} \quad R^2 = 0.8454 \tag{27}$$

Considering the adsorption effect, the critical shift phenomena is now modeled better and more realistic than the previous work (Zarragoicoechea and Kuz 2002) which was developed for neutral pore walls.

Results and discussion

Hysteresis critical temperature, T_{ch}

As illustrated in Fig. 6 (Morishige and Shikimi 1998), Hysteresis Critical Temperature (T_{ch}) [K] is the temperature above which the hysteresis loop vanishes in adsorption–desorption diagrams. Moreover, the jump in the adsorption curve associated with capillary condensation decreases as the temperature rises and eventually disappears at Pore Critical Temperature (T_{cp}) [K] that is higher than T_{ch} (Morishige and Shikimi 1998). As it has been followed previously (Zarragoicoechea and Kuz 2002), Eqs. (21) and (22) are supposed to calculate T_{ch}.

Table 2 shows the values of C_0 to C_2 (coefficients of Eq. (8)) for argon, nitrogen, oxygen, carbon dioxide, xenon, and ethylene. To make an in-depth clarification, the numerical values and their nonlinear fitted curves are presented in Fig. 7 and compared to those of Lennard–Jones (Zarragoicoechea and Kuz 2002).

Calculated T_{ch} values from this study are listed in Table 3 and compared with the corresponding L-J outputs as well as the empirical reports. Employing the Kihara potential function, we observe that results are more satisfactory and much closer to the experimental values, whereas the L-J model has led to far inaccurate predictions. For all components studied in this section, the overall error improvement was almost 9 percent on average. The highest and lowest improvements belonged to CO_2 (19.67%) and Ar (0.18%), respectively. Nevertheless, CO_2, O_2, and Xe still have great deviation from empirical measurements of T_{ch}, even though our model is more physically realistic than the L-J model. Two factors can account for such a deviation; uncertainties in experimental reports, and incapability of both potential functions to express extreme flexibility in modeling. Regarding the latter, although the Kihara potential is much more flexible in terms of mathematical modeling, both potential functions are merely a representative and approximation of the real potential behavior of two interactive molecules

Table 1 Values of coefficients in the adsorption thickness equation utilized in this work

	N_2	CO_2	CH_4	C_2H_6	C_3H_8	n-C_4H_{10}	n-C_5H_{12}	n-C_6H_{14}	n-C_7H_{16}	n-C_8H_{18}	n-C_9H_{20}	n-$C_{10}H_{22}$
a	0.4441	0.8646	0.4848	0.7678	0.8601	0.9029	0.9543	0.8985	0.9178	0.9136	0.9139	0.9218
b	0.0239	0.1009	0.0288	0.0748	0.0949	0.1051	0.1257	0.1033	0.1080	0.1062	0.1071	0.1096
c	0.6594	0.7955	0.6520	0.6465	0.6687	0.6338	0.7231	0.5655	0.5526	0.5209	0.5203	0.5048
$d(\times 10^{-5})$	−3.849	−0.435	−3.695	−1.809	−1.462	−1.620	−0.867	−1.535	−1.422	−1.371	−1.143	−1.393
R^2	0.9997	0.9999	0.9996	0.9997	0.9998	0.9997	0.9999	0.9996	0.9996	0.9996	0.9995	0.9995

Fig. 5 Measured and fitted values of adsorption thickness
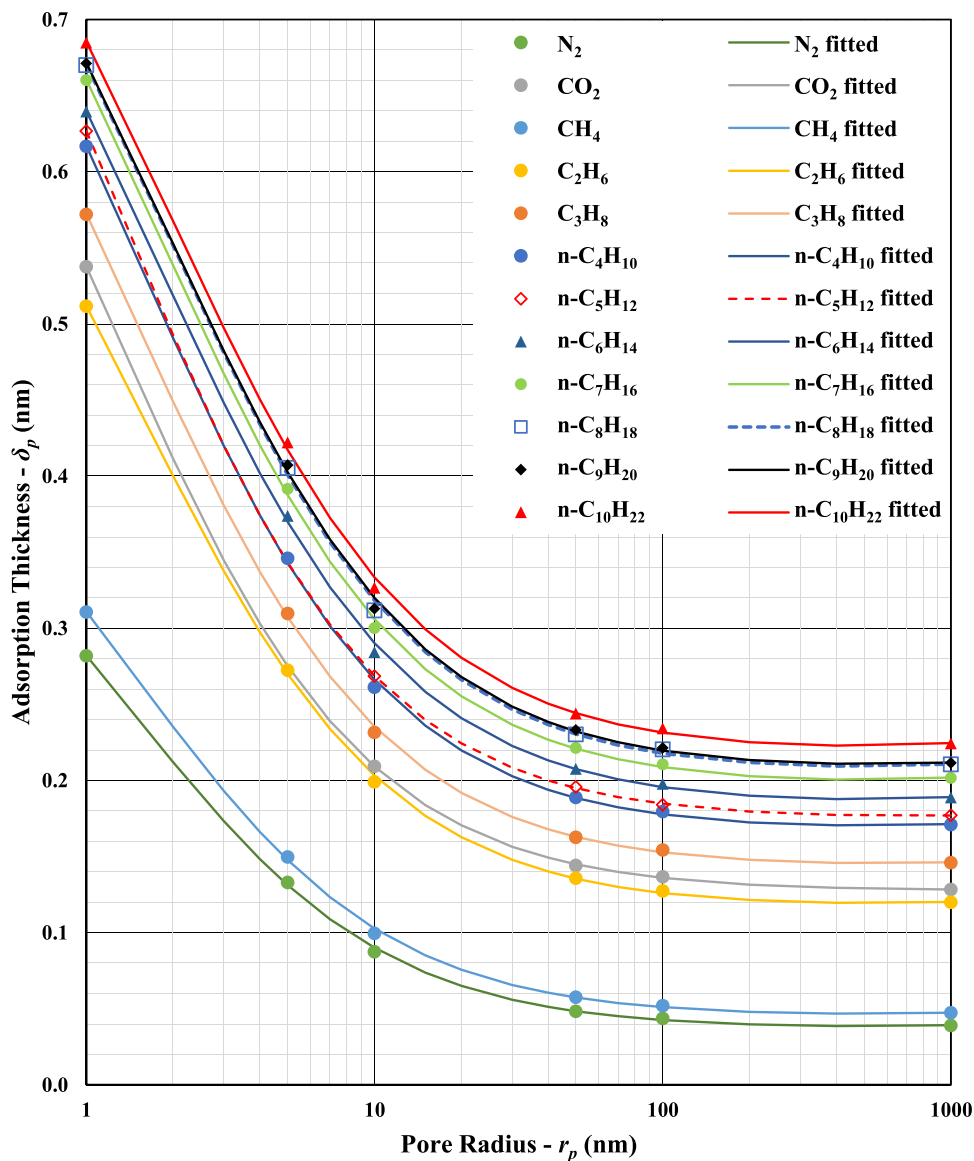
Fig. 6 Adsorption/desorption volume versus relative fugacity for argon at 2.1 nm
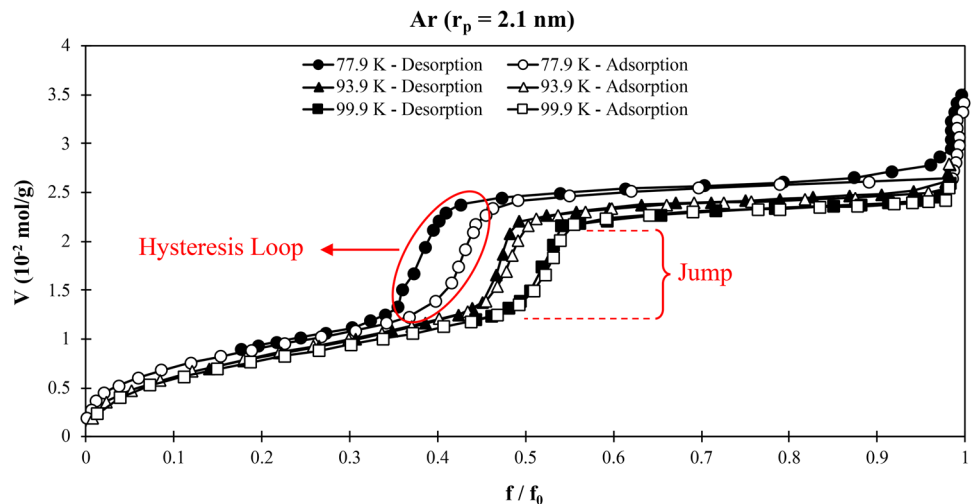
Table 2 Values of C_0 to C_2 for argon, nitrogen, oxygen, carbon dioxide, xenon and ethylene

Components	C_0	C_1	C_2
Ar	− 2.354	3.816	− 1.697
N_2	− 1.956	2.849	− 1.095
O_2	− 1.825	2.594	− 0.962
C_2H_4	− 1.925	2.788	− 1.063
CO_2	− 1.312	1.654	− 0.498
Xe	− 2.314	3.594	− 1.507

(Prausnitz et al. 1998). Hence, they may lead to erroneous results for some fluids whose true potential behavior is far different from them. On the other hand, T_{ch} is a concept to which only a few research works have turned their attention (Morishige and Ito 2002; Morishige and Shikimi 1998; Morishige et al. 2003), and there is no crystal-clear explanation for its true nature.

Pore critical temperature, T_{cp}

We followed the same procedure of the previous section herein for nitrogen, carbon dioxide, and normal alkanes including methane, ethane, propane, n-butane, and n-octane. Due to having a decent molecular weight disparity, these components are a superb representative of n-alkanes and their behavior to be studied in nano-scale pores. As we

discussed earlier, the essential point is that the application of Kihara potential provides specific values of C coefficients for each type of fluid (Table 4) rather than the unique constants of the Lennard–Jones. For convenience, Eqs. (28) and (29) are proposed as a function of C_0 for values in Table 4, with $R^2 = 1$.

$$C_1\left(a_k^*\right) = 0.158 \times C_0\left(a_k^*\right)^2 - 1.3081 \times C_0\left(a_k^*\right) - 0.2264 \tag{28}$$

$$C_2\left(a_k^*\right) = -0.1485 \times C_0\left(a_k^*\right)^2 + 0.4126 \times C_0\left(a_k^*\right) + 0.1902 \tag{29}$$

When the pore cross section goes to infinity and the fluid is not confined anymore, it is totally expected that Eqs. (21) and (22) must result in the bulk critical temperature (T_C) and pressure (P_c), or $T_{cp}(r = \infty) = T_C$ and $P_{cp}(r = \infty) = P_c$. Nonetheless this will not take place and the approach developed for T_{ch} must be adjusted, accordingly. Although this issue is tackled via a critical shift correlation for the L-J model (Zarragoicoechea and Kuz 2004), here we offer and follow a thermodynamic-based perspective in which a^* and b^* must be equal to the vdW constants a_{vdW} and b_{vdW}, respectively. This will manipulate the Kihara parameters until the demanded equality between T_{cp} (P_{cp}) at $r = \infty$ and T_c (P_c) is achieved.

Being a three-parameters potential function, the Kihara model also needs a third equation for the adjustment procedure, $a_k^* = f(\omega)$, where ω is the acentric factor. Furthermore,

Fig. 7 Numerical solution to Eq. (8) for Ar, O_2, C_2H_4, CO_2 and their fitted curves as well as that of the Lennard–Jones model
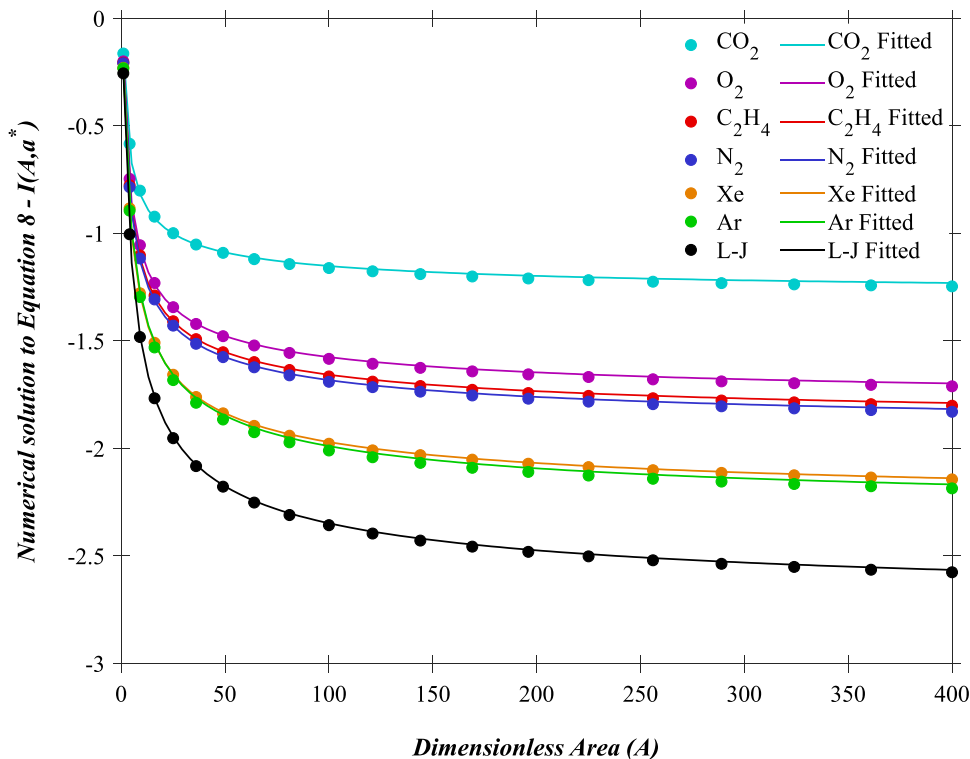
Table 3 Calculated hysteresis critical temperatures of Ar, N_2, O_2, C_2H_4, CO_2, and Xe plus those of the Lennard–Jones model and the experimental reports

r_p	Ar			CO_2			O_2		
nm	Kihara[a] (K)	L–J[b] (K)	T_{ch}[c] (K)	Kihara[a] (K)	L-J[b] (K)	T_{ch}[c] (K)	Kihara[a] (K)	L-J[b] (K)	T_{ch}[c] (K)
1.2	71.5	71.7	62	148.7	111.3	156	81.6	64.3	64
1.4	74.7	74.8	74	153.7	117.3	173	84.3	67.2	76
1.8	79.2	79.1	87	160.5	125.7	195	88.1	71.2	91
2.1	81.4	81.3	100	164	130	215	90	73.3	102
AARD[d]	10.95	11.13		14.31	33.98		13.34	15.49	
r_p	C_2H_4			N_2			Xe		
nm	Kihara[a] (K)	L–J[b] (K)	T_{ch}[c] (K)	Kihara[a] (K)	L–J[b] (K)	T_{ch}[c] (K)	Kihara[a] (K)	L–J[b] (K)	T_{ch}[c] (K)
1.4	141.7	116.3	130	62.3	55	57			
1.8	149.8	125.3	148	65.6	58.5	68			
1.9				66.2	60.5[*]	68[**]			
2.1	154.1	129.9	163	67.2	60.3	76			
2.52							189.6	149	251.3
3.66							196.2	156.7	259.8
AARD	5.22	15.4		6.75	12.3		24.51	40.19	

[a]This study, calculated based on Kihara parameters from (Tee et al. 1966a, b)

[b]From (Zarragoicoechea and Kuz 2002)

[c]From (Morishige and Shikimi 1998)

[d]Average Absolute Relative Deviation (%)

[*]Calculated based on L-J parameters from (Tee et al. 1966a, b)

[**]From (Morishige et al. 2003)

Table 4 Values of C_0 to C_2 for CH_4, C_2H_6, C_3H_8, n-C_4H_{10}, and n-C_8H_{18}

Components	C_0	C_1	C_2
CH_4	−1.886	2.803	−1.116
C_2H_6	−1.800	2.639	−1.033
C_3H_8	−1.532	2.148	−0.790
n-C_4H_{10}	−1.284	1.713	−0.584
n-C_8H_{18}	−0.729	0.811	−1.879

Table 5 Adjusted Kihara parameters of normal alkanes

Components	a_k	σ_k	ε_k
	($\times 10^{-10}$m)	($\times 10^{-10}$m)	K
CH_4	0.356	3.255	353.3
C_2H_6	0.454	3.742	591.1
C_3H_8	0.672	4.201	825.2
n-C_4H_{10}	0.919	4.618	1096.5
n-C_5H_{12}	1.129	5.018	1334.5
n-C_6H_{14}	1.374	5.418	1604.1
n-C_7H_{16}	1.538	5.771	1798.3
n-C_8H_{18}	1.879	6.226	2150.1

it seems that the value of a_k^* remains fixed for every fluid, and it comes from one of the previous works for Kihara parameters (Tee et al. 1966a, b) in which the value of $2a_k/(\sigma_k - 2a_k)$ has been determined through numerical curve fittings of $B(T)$ and/or viscosity (μ) data.

Adjusted Kihara parameters of normal alkanes from CH_4 to n-C_8H_{18} are brought in Table 5.

The microscopic and macroscopic theories of the corresponding states could be related by establishing a connection between one theory's parameters and those of the other. In the former theory, there are two independent parameters (energy and distance parameters), and in the latter, there appear to be three (v_c, T_c, and P_c). Yet, in fact, only two of these are independent since the compressibility factor at the critical point

(z_c) is the same for all fluids (Prausnitz et al. 1998). For a fluid at a characteristic state, where the liquid and the gaseous phases become identical, the critical temperature is a measure of kinetic energy; Hence, a relation between ε_k and T_c seems quite reasonable. Identically, the critical molar volume (v_c) represents the molecular size, and proportionality between σ_k^3 or a_k^3 and v_c also seems to be reasonable (Prausnitz et al. 1998). Thus, Eqs. (30) to (32) are developed to be used as alternative correlations for the values listed in Table 5, with the average R^2 of 0.993,

$$\frac{a_k}{\sqrt[3]{v_c}} = -26.834\omega^3 + 20.26\omega^2 + 0.1882\omega + 0.743 \quad (30)$$

$$\frac{\sigma_k}{\sqrt[3]{v_c}} = 6.3389\omega^3 + 1.1671\omega^2 + 0.6967\omega + 7.0352 \quad (31)$$

$$\frac{\varepsilon_k}{T_c} = -28.888\omega^3 + 24.225\omega^2 - 0.336\omega + 1.8308 \quad (32)$$

where T_c and v_c are the bulk critical temperature [K] and volume [$m^3 \cdot Kgmol^{-1}$], respectively, and a_k and σ_k both are in angstrom.

Tables 6, 7, 8 present the calculated pore critical temperatures of N_2, CO_2, CH_4, C_2H_6, C_3H_8, n-C_4H_{10}, and

n-C_8H_{18}, and compares them to those of the Lennard–Jones as well as the literature reported values. Therein, this study has ameliorated the average overall error of normal alkanes by 6.4%. The overall mean error of this work was less than 2.5%, whereas that of the Lennard–Jones was 8.11%. Note that the highest and the lowest improvements belong to heavier normal alkanes (n-C_4H_{10} and n-C_8H_{18}) and non-hydrocarbons, respectively.

Overall, it is noticeable that in smaller pore radii, T_{cp} values calculated by the L–J model decrease dramatically, while our model has a more rational reduction. Such a reasonable behavior accounts for our lower deviation in smaller pore sizes for most of the fluids.

For CH_4, C_2H_6, n-C_4H_{10}, and n-C_8H_{18}, T_{cp} reports were available from various research studies. Regarding the

Table 6 Comparison among the calculated T_{cp} values of CH_4, n-C_4H_{10}, and n-C_8H_{18} based on their adjusted Kihara parameters as well as those of the adjusted L-J model and the reported data

r_p	CH_4 (Mica)			r_p	n-C_4H_{10} (Mica)			r_p	n-C_8H_{18} (Mica)		
nm	Kihara[a] (K)	L–J[b] (K)	T_{cp}[c] (K)	nm	Kihara[a] (K)	L–J[b] (K)	T_{cp}[c] (K)	nm	Kihara[a] (K)	L–J[e] (K)	T_{cp}[c] (K)
4.23	178.5	174.6	182.3	4.28	391.3	370.4	397.5	5.54	529.1	498.4	530.4
3.21	174.7	169.8	176.6	3.26	381.0	354.1	382.7	4.41	519.3	481.3	516.0
2.69	171.3	165.9	171.3	2.71	372.3	340.5	374.6	3.30	503.0	453.5	503.8
2.15	167.2	160.0	164.7	2.17	359.9	321.4	359.3	2.20	471.6	401.7	466.9
1.63	160.1	150.9	152.4	1.64	339.8	291.0	331.2	1.66	441.6	354.3	429.4
AARD	2.00	3.01			1.08	9.21			0.97	10.84	
r_p	CH_4 (Graphite)			r_p	n-C_4H_{10} (Graphite)			r_p	n-C_8H_{18} (Graphite)		
nm	Kihara[a] (K)	L–J[b] (K)	T_{cp}[d] (K)	nm	Kihara[a] (K)	L–J[b] (K)	T_{cp}[d] (K)	nm	Kihara[a] (K)	L-J[e] (K)	T_{cp}[d] (K)
4.14	178.2	174.3	183.4	4.17	390.4	369.0	402.1	5.28	527.2	495.9	540.6
3.15	174.4	169.4	177.9	3.19	380.0	352.5	389.8	4.25	517.4	479.2	531.7
2.61	171.2	165.2	174.3	2.68	371.8	339.7	379.0	3.22	501.4	452.2	513.9
2.11	166.8	159.5	169.0	2.15	359.3	320.4	361.6	2.17	470.1	401.1	470.7
1.62	159.9	150.6	152.2	1.63	339.6	290.6	324.2	1.65	441.0	355.5	416.6
AARD	2.58	4.33			2.54	9.98			2.71	11.92	
r_p	CH_4			r_p	C_3H_8			r_p	CO_2		
nm	Kihara[a] (K)	L-J[b] (K)	T_{cp}[f, g] (K)	nm	Kihara[a] (K)	L-J[c] (K)	T_{cp}[g] (K)	nm	Kihara[a] (K)	L-J[e] (K)	T_{cp}[h] (K)
10	185.4	183.4	186.0	2.034	311.9	294.2	320.8	8.145	294.9	288.9	303.0
7	183.2	180.4	183.3	AARD	2.77	8.29		6.079	291.7	283.8	301.3
2.034	165.9	157.0	169.7[g]	r_p	n-C_4H_{10}			4.57	287.7	277.2	294.5
				nm	**Kihara[a]** (K)	**L–J[b]** (K)	T_{cp}[g](K)				
				2.034	355.7	297.2	372.0				
AARD	0.89	3.48		AARD	4.39	20.12		AARD	2.72	5.45	

[a]This study, calculated based on adjusted Kihara parameters listed on Table 5

[b]Calculated based on L–J parameters from (Tee et al. 1966a, b)

[c,d]From (Singh et al. 2009)

[e]Calculated based on L–J parameters from (Hirschfelder et al. 1964)

[f]From (Jin and Nasrabadi 2016)

[g]From (Jiang et al. 2004)

[h]From (Tan et al. 2019)

Table 7 Comparison among calculated T_{cp} of C_2H_6 from this study, adjusted L-J, and the reported values

r_p	C_2H_6		
nm	Kihara[a] (K)	L–J[b] (K)	T_{cp}(K)
2.034	260.8	236.5	269.5[c]
3	271.7	257.6	258.0[d]
4	282.2	269.1	281.5[d]
4.57	285.1	273.5	297.5[e]
5	286.7	276.1	292.0[d]
5	286.7	276.1	285.1[f]
6	289.8	280.9	298.0[d]
6	289.8	280.9	292.5[f]
6.079	290.1	281.2	304.1[e]
7	292.0	284.3	300.0[d]
7	292.0	284.3	291.9[g]
8	293.6	286.9	302.0[d]
8.145	293.9	287.2	304.6[e]
9	294.9	288.9	304.0[d]
10	296.0	290.5	296.2[f]
AARD	2.38	5.08	

[a]This study, calculated based on adjusted Kihara parameters listed on Table 5

[b]Calculated based on L-J parameters from (Tee et al. 1966a, b)

[c]From (Jiang et al. 2004)

[d]From (Pitakbunkate et al. 2016)

[e]From (Tan et al. 2019)

[f]From (Lowry and Piri 2018)

[g]From (Jin and Nasrabadi 2016)

Table 8 Comparison among calculated T_{cp} of N_2 from this study, the adjusted L-J, and the reported values

r_p	N_2		
nm	Kihara[a] (K)	L-J[b] (K)	T_{cp}[c] (K)
1.2	95.02	92.49	87
1.9	103.86	104.23	98.12
2.2	105.99	107.09	103
3	109.64	112.02	105
3.2	110.27	112.88	105
3.9	111.99	115.21	112
AARD	4.57	5.59	

[a]This study, calculated based on adjusted Kihara parameters

[b]Calculated based on L–J parameters from (Tee et al. 1966a, b)

[c]From (Morishige and Shikimi 1998; Morishige et al. 2003)

values from Singh et al. (2009), generally, our calculations were closer to T_{cp} values of mica porous media. Regarding CH_4, however, the least deviation was achieved when we compared our calculations to the reports from the work of Jin and Nasrabadi (2016), wherein the porous media was,

interestingly, made out of graphite. Although the systems studied in different works have different conditions, the results for CH_4 denotes that T_{cp} values generated by our model is closer to graphite porous media in larger pore radii, and to those of mica in smaller ones.

According to the T_{cp} reports of C_2H_6 for which the largest number of data points were available, our calculations were closer to measurements except for one pore radius, 3 nm, reported by Pitakbunkate et al. (2016) for graphite porous media. Considering all the data points from their study, the value of pore critical temperature witnessed a drastic reduction from 4 to 3 nm, which was a behavior similar to that of the L–J model in smaller pore sizes.

As a general note, both models underestimate a fluid's pore critical temperature. Yet, this underestimation is much more severe in the L–J model and the approach proposed in this study succeeded in addressing this issue by employing a more physically realistic potential function and a better adjustment method to calculate T_{cp}.

Figures 8 and 9 reveal for the assessed fluids that how much this study generated better results, compared with the adjusted L-J model. Besides, the adjusted Kihara parameters of components in Sect. "Results and discussion" are presented in Table 9. Equations (33) to (35) may also be alternatively employed with an average R^2 of 0.9983 for the values of this table, excluding xenon.

$$\frac{a_k}{\sqrt[3]{v_c}} = 10.7365 - \frac{12.854}{1+\omega} + \frac{2.8788}{1 + 9.4694\omega - 0.00075\omega^2} \tag{33}$$

$$\frac{\sigma_k}{\sqrt[3]{v_c}} = 8.67913 - \frac{1.7357}{1+\omega} + \frac{1.9238}{1 + 1933.51\omega + 33.849\omega^2} \tag{34}$$

$$\frac{\varepsilon_k}{T_c} = 9.2272 - \frac{8.3714}{1+\omega} + \frac{2.99046}{1 + 111.332\omega + 0.497007\omega^2} \tag{35}$$

Tuning versus curve fitting

Phase behavior models based on the aforementioned equations may not lead to accurate predictions, even for a well characterized (adjusted) model proposed in the previous section. Hence, in order to have precise results, we will calibrate or tune the model's parameters against experimental data generated at pertinent conditions for specific studies. Here we manually tune the Kihara parameters for n-alkanes studied in this research, predicting the reported pore critical temperatures with the maximum precision. In favor of three adjustable parameters, the Kihara potential function is entirely flexible to be manipulated for almost all fluids (Tee et al. 1966a, b). Nevertheless, this approach affects the bulk critical temperature calculations when the
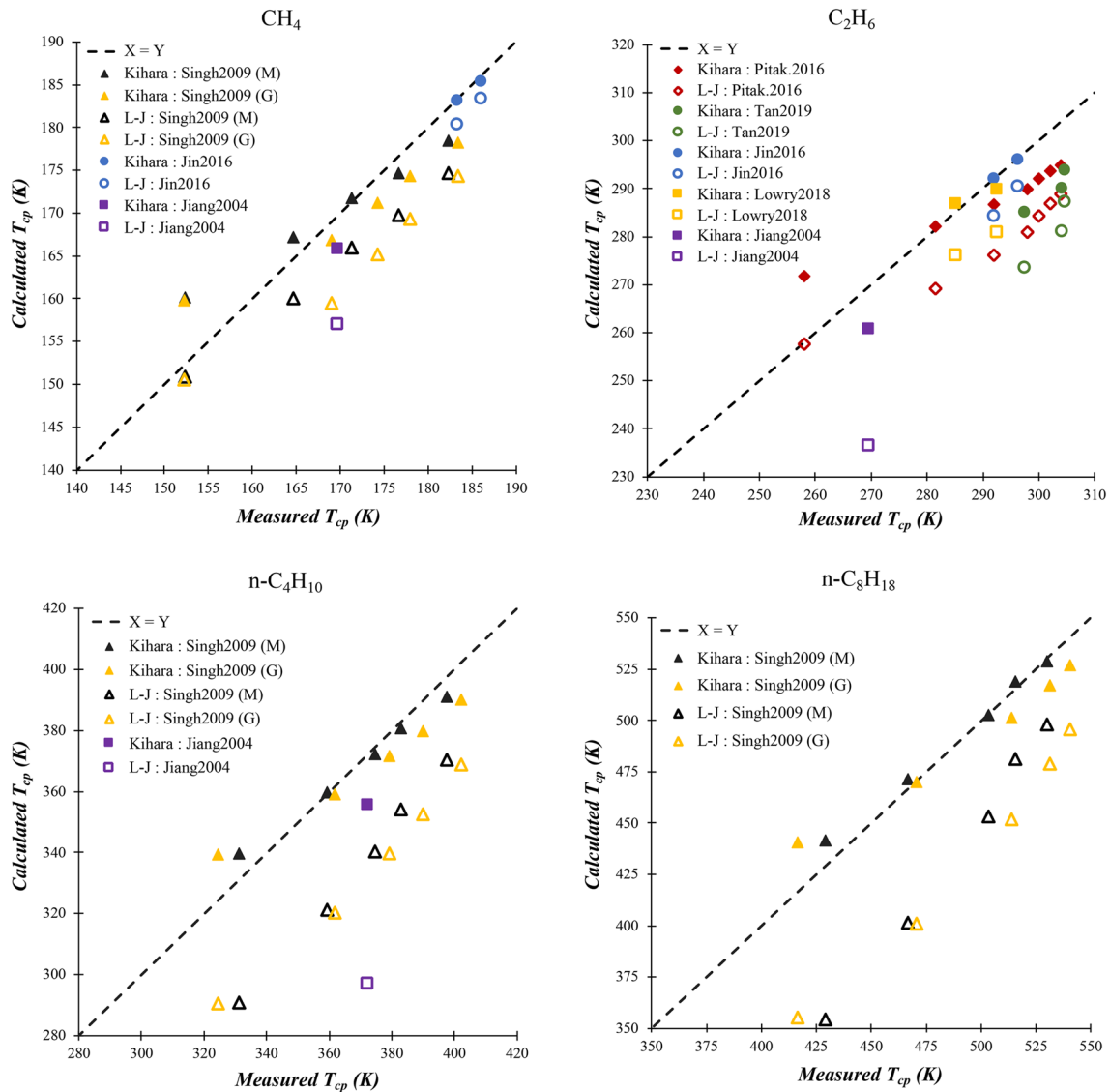
Fig. 8 Cross plots of calculated T_{cp} versus measured T_{cp} for CH_4, C_2H_6, n-C_4H_{10}, and n-C_8H_{18}. Filled symbols represent this work

pore size goes to infinity (details in Supporting Information). Table 10 shows the tuned Kihara parameters for N_2, CO_2, CH_4, C_2H_6, n-C_4H_{10}, and n-C_8H_{18}. Noteworthy it is that the Kihara parameters of CH_4, n-C_4H_{10}, and n-C_8H_{18} are tuned based on their Mica type T_{cp} measurements (Singh et al. 2009) (because of more sensible trend), and those of C_2H_6, CO_2, and N_2 based on the experimental measurements (Morishige and Shikimi 1998; Morishige et al. 2003; Tan et al. 2019).

With the tuned parameters, the pore critical temperature was calculated once again. From results shown in Tables 11 and 12, the overall error of our approach for n-alkanes was near 0.4%.

In recent years, various measures have been taken in order to optimize the Lennard–Jones critical temperature shift equation via curve fitting of experimental values in the literature. The most renowned ones are as follows:

$$1 - \frac{T_{cp}}{T_c} = 0.8493 \left(\frac{r_p}{\sigma_{LJ}} \right)^{-1.241} + 0.015 \quad \text{(Jin et al. 2013)}$$

$$\text{(36)}$$

$$1 - \frac{T_{cp}}{T_c} = 3.374 \times \left(\frac{r_p}{\sigma_{LJ}} \right)^{-1.637} \quad \text{(Yang et al. 2019)} \quad \text{(37)}$$
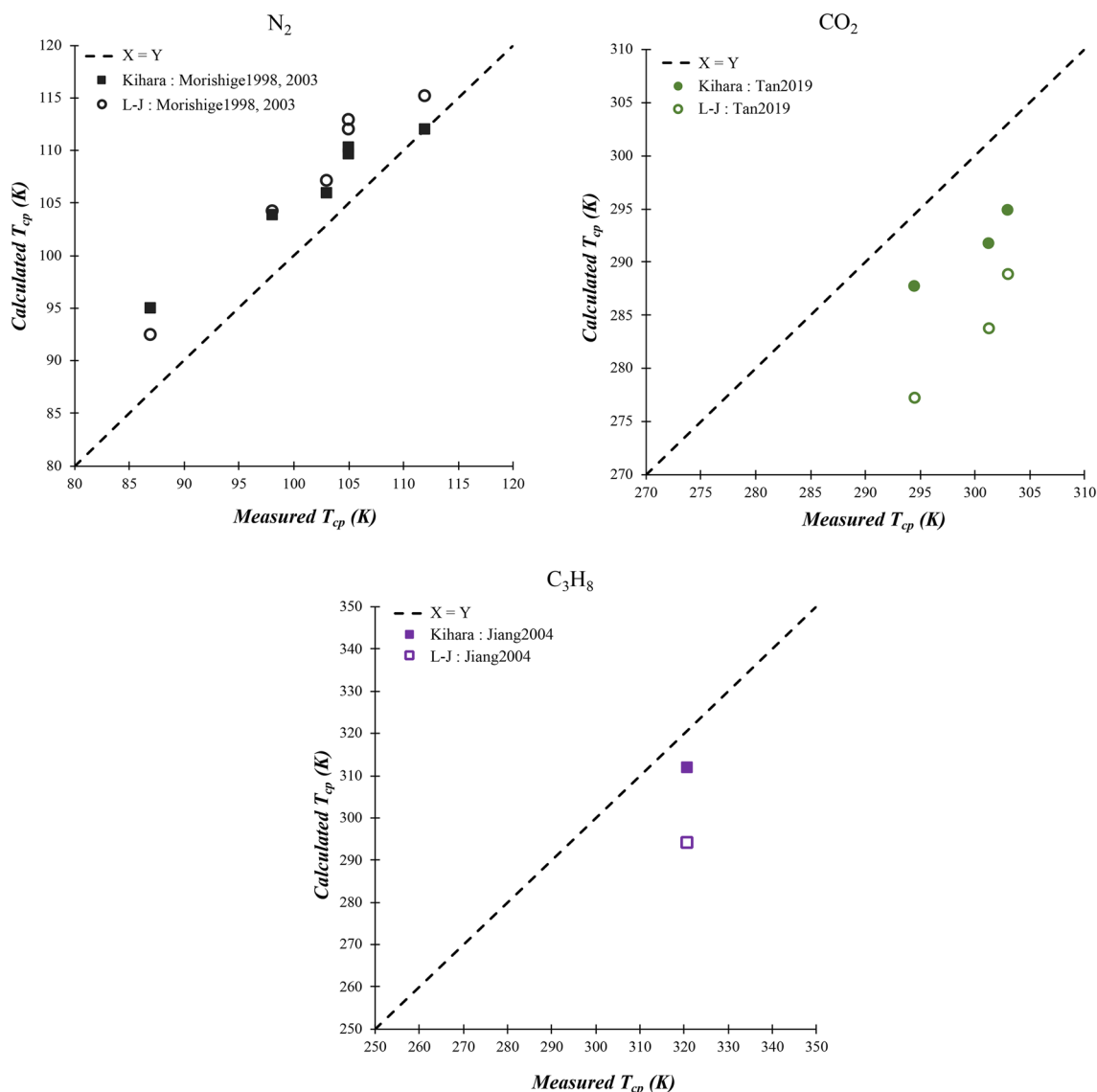
Fig. 9 Cross plots of calculated T_{cp} versus measured T_{cp} for N_2, CO_2, and C_3H_8. Filled symbols represent this work

Table 9 Adjusted Kihara parameters of Ar, N_2, O_2, CO_2, C_2H_4 and Xe

Components	a_k ($\times 10^{-10}$m)	σ_k ($\times 10^{-10}$m)	ε_k K
Ar	0.433	3.739	579.5
N2	0.314	3.137	213.7
O2	0.347	2.947	296.9
CO2	0.635	3.302	765.7
C2H4	0.375	3.600	513.7
Xe	0.231	3.447	461.6

Table 10 Tuned Kihara parameters of CH_4, C_2H_6, n-C_4H_{10}, and n-C_8H_{18}

Components	a_k ($\times 10^{-10}$m)	σ_k ($\times 10^{-10}$m)	ε_k K
CO2	0.5250	3.670	661.29
N2	0.4286	4.286	216.09
CH4	0.4187	5.098	342.02
C2H6	0.2800	3.655	525.84
n-C4H10	1.4917	6.321	1312.1
n-C8H18	2.1662	7.175	2188.9

Table 11 Calculated pore critical temperatures of CH_4, C_2H_6, n-C_4H_{10}, and n-C_8H_{18} based on their tuned Kihara parameters

r_p nm	CH_4 Kihara[a] (K)	T_{cp}[b] (K)	r_p nm	n-C_4H_{10} Kihara[a] (K)	T_{cp}[b] (K)	r_p nm	n-C_8H_{18} Kihara[a] (K)	T_{cp}[b] (K)
4.23	182.9	182.3	4.28	397.7	397.5	5.54	532.7	530.4
3.21	176.6	176.6	3.26	383.9	382.7	4.41	521.1	516.0
2.69	171.7	171.3	2.71	372.4	374.5	3.30	502.1	503.8
2.15	164.2	164.7	2.17	356.0	359.3	2.20	465.7	466.9
1.63	152.6	152.4	1.64	329.5	331.2	1.66	431.1	429.4
AARD	0.21			0.48			0.48	

[a]This study, calculated based on the tuned Kihara parameters listed on Table 10

[b]From (Singh et al. 2009), Mica

Table 12 Calculated pore critical temperatures of N_2, CO_2, and C_2H_6 based on their tuned Kihara parameters

r_p nm	N_2 Kihara[a] (K)	T_{cp}[b] (K)	r_p nm	CO_2 Kihara[a] (K)	T_{cp}[c] (K)	r_p nm	C_2H_6 Kihara[a] (K)	T_{cp}[d] (K)
3.9	109.6	112	8.145	303.9	303.0	8.145	306.8	304.6
3.2	107.3	105	6.079	300.2	301.3	6.079	302.7	304.1
3.0	106.5	105	4.570	295.2	294.5	4.570	297.3	297.5
2.2	101.6	103				2.034	271.4	269.5
1.9	98.71	98.12						
1.2	87.06	87						
AARD	1.30			0.32			0.48	

[a]This study, calculated based on the tuned Kihara parameters listed on Table 10

[b]From (Morishige and Shikimi 1998; Morishige et al. 2003)

[c]From (Tan et al. 2019)

[d]From (Jiang et al. 2004; Tan et al. 2019)

$$1 - \frac{T_{cp}}{T_c} = 1.7391 \times \left(\frac{r_p}{\sigma_{LJ}}\right)^{-1.379} \quad \text{(Yang and Li 2020)}$$

(38)

$$1 - \frac{T_{cp}}{T_c} = 0.6794 \times \left(\frac{r_p}{\sigma_{LJ}}\right)^{-0.7878} \quad \text{(Song et al. 2020)}$$

(39)

The flexibility of Kihara potential provided us with the most precise predictions in favor of our tuning approach. Despite numerical curve fittings in which only the constants in the critical shift equation vary, here for the very first time, we dedicated a specific set of values for each component (Table 10), trying to make the results perfectly matched to the real pore critical temperatures (Figs. 10 and 11). Yet, a_k^* values has been kept equal to its reported ones (Tee et al. 1966a, b) in order to achieve rational outcomes. Although our adjusted Kihara method is only based on thermodynamic adjustments, it is surprisingly able to generate better results rather than the aforementioned L–J correlations (details in the Supporting Information).

Although the correlation presented by Jin et al. (2013) is the oldest model included in this section, it performed better than the newer models of Yang and Li (2020) and Song et al.

(2020) almost for all fluids except for nitrogen. This can be attributed to the fact that the diversity of fluids studied in the work of Jin et al. was much wider than other ones. In fact, the recent models were mostly developed based on T_{cp} reports of methane. That is why the four correlations in this section perform roughly the same for CH_4. This is much more conspicuous for the correlation proposed by Song et al., when applied for other fluids than CH_4.

Capillary condensation–Maxwell construction

In thermodynamic equilibrium, a necessary condition for stability is that pressure does not increase with volume. This basic consistency requirement is sometimes violated in analytic models for first order phase transitions, such as that of vdW-type EOSs (Danesh 1998). The occurrence of this violation in P–V diagrams of vdW-type EOSs is known as capillary condensation (Zarragoicoechea and Kuz 2002).

The vdW P–V isotherm diagram of the Lennard–Jones model has been evaluated in the literature (Zarragoicoechea and Kuz 2002). In this section, we investigate whether capillary condensation will form in vdW and PR EOSs' P–V diagrams when the EOS is associated with the Kihara potential function. As illustrated in Fig. 12 for vdW, the Maxwell
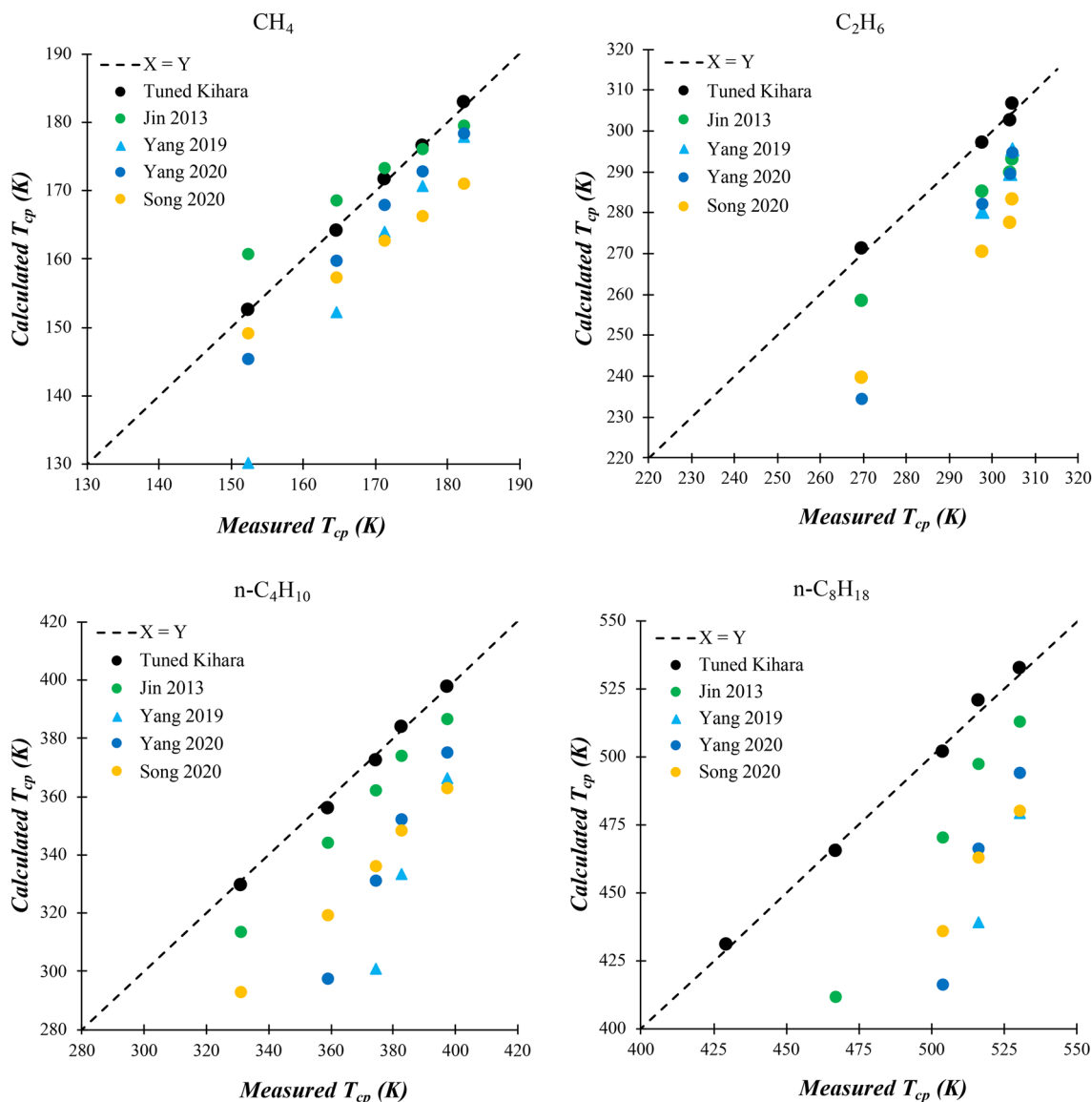
Fig. 10 Cross plots of calculated T_{cp} versus measured T_{cp} for CH_4, C_2H_6, n-C_4H_{10}, and n-C_8H_{18}

construction is utilized to acquire the gas–liquid coexistence dashed line in the two-phase region where $P_{zzL} = P_{zzV}$. It is worth mentioning that the critical shift is applied in the EOS through substituting $T_c = T_{cp}$ and $P_c = P_{cp}$.

Nonetheless, the controversial subject here is the P–V diagrams of PR EOS as the most widely applied equation in the industry (Danesh 1998). It is has been reported that a confined fluid will be in its supercritical state when PR is coupled with L–J (Islam et al. 2015), whereas the vdW EOS gives capillary condensation at the same bulk reduced temperature ($T_r = T/T_c$); therefore, the predicted state of the fluid is not supercritical.

To address this for the Kihara potential function, first, the critical-shift-associated form of PR EOS must be driven, which is explained as follows (Peng and Robinson 1976):

$$P = \frac{RT}{v - b_{PR}} - \frac{a_{PR}}{v(v + b_{PR}) + b_{PR}(v - b_{PR})} \tag{40}$$

where

$$a_{PR} = 0.45724 \frac{(RT_c)^2}{P_c} \alpha(T) \tag{41}$$

$$b = 0.0778 \frac{RT_C}{P_c} \tag{42}$$

$$\alpha(T) = \left(1 + m\left(1 - \sqrt{T_r}\right)\right)^2 \tag{43}$$
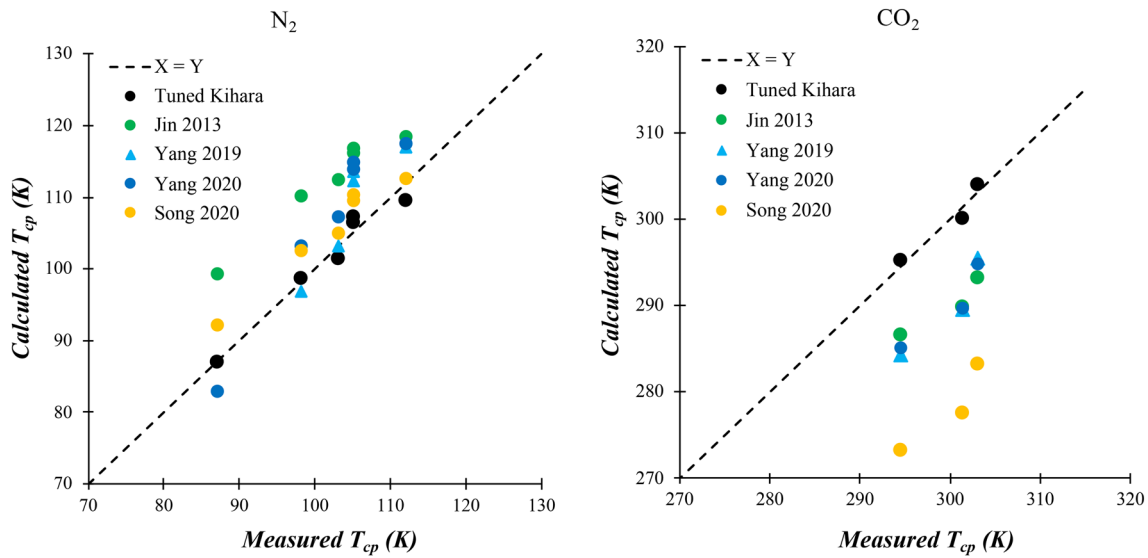
Fig. 11 Cross plots of calculated T_{cp} versus measured T_{cp} for N_2 and CO_2
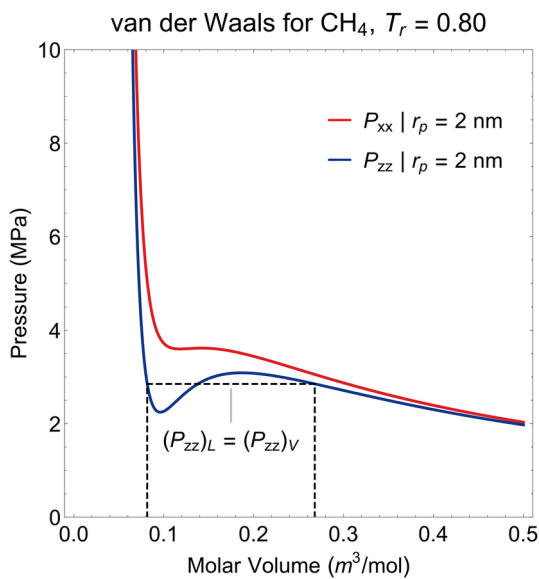
Fig. 12 Capillary condensation of vdW EOS for methane in axial section (P_{zz}) at $T_r = 0.8$ and $r_p = 2$ nm

$$m = 0.37464 + 1.54226\omega - 0.26992\omega^2 \tag{44}$$

where a_{PR} and b_{PR} are EOS constants; v is molar volume [m^3.Kgmol^{-1}]; T_c [K] and P_c [MPa] are critical temperature and pressure; T_r is the bulk reduced temperature; w is the acentric factor; and R is the universal gas constant [m^3.MPa.K^{-1}. Kg mol^{-1}]. To apply the critical shift effect, similar to vdW, T_c and P_c must be recalculated through Eqs. (21) and (22), based on the adjusted Kihara parameters, and C coefficients.

Afterward, we comprehended that the PR EOS, when coupled with the Kihara potential, can demonstrate capillary condensation as the temperature declines. As Fig. 13 reveals, for methane and carbon dioxide at a given reduced temperature and pore size, the confined fluid is homogenous with respect to various axial and transverse pressures $P_{zz} < P_{xx}$.

Elaborating further, we are well provided with the commencement of the confinement effect on the phase behavior of fluids, designated by the purple-dashed lines in Fig. 13. For instance, at almost the same T_r, carbon dioxide is under confinement at larger pores (10 to 20 nm) than methane, which feels the critical shift in pore sizes of less than 5 to 10 nm. Such a concept could be directly related to the higher a_k value of CO_2, forbidding the molecules to excessively approaching each other rather than the CH_4 ones, which are further allowed in interpenetration. At this step, our results are similar to those of Islam et al. (2015), but further evaluation reveals the differences.

Decreasing the temperature and maintaining the transverse pore area constant where T is less than T_{cp} at 2 nm, we observe a loop appearing for the axial pressure P_{zz} (Fig. 14). If we take the temperature even lower, the transverse pressure also begins to presents a loop along with the axial part (Fig. 15), which indicates that in contrast to the reports of Islam et al. (2015), both vdW and PR EOSs manifest capillary condensation in the axial part at the same reduced temperature.

To provide a superior perspective of the phase behavior, Fig. 16 is presented to show and compare the 3D Pressure–Volume-Temperature diagrams of CH_4 and CO_2 for the axial pressure generated by PR EOS, in which the red and
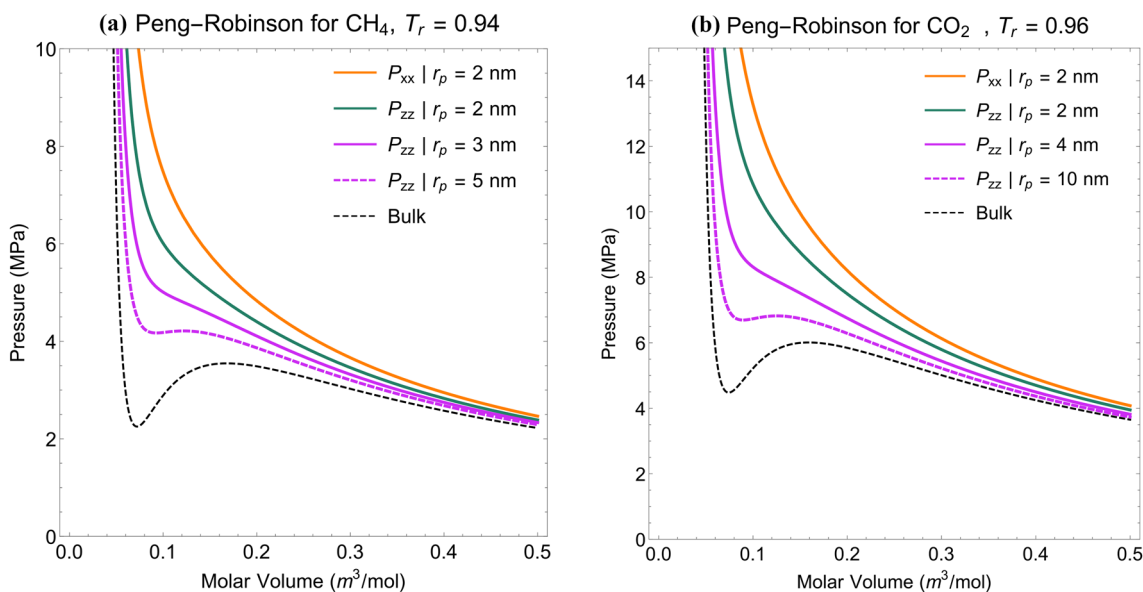
Fig. 13 Volume dependence of the axial (P_{zz}) and transverse (P_{xx}) pressure tensor components for **a** methane at $T_r = 0.94$ and **b** carbon dioxide at $T_r = 0.96$ in different pore sizes
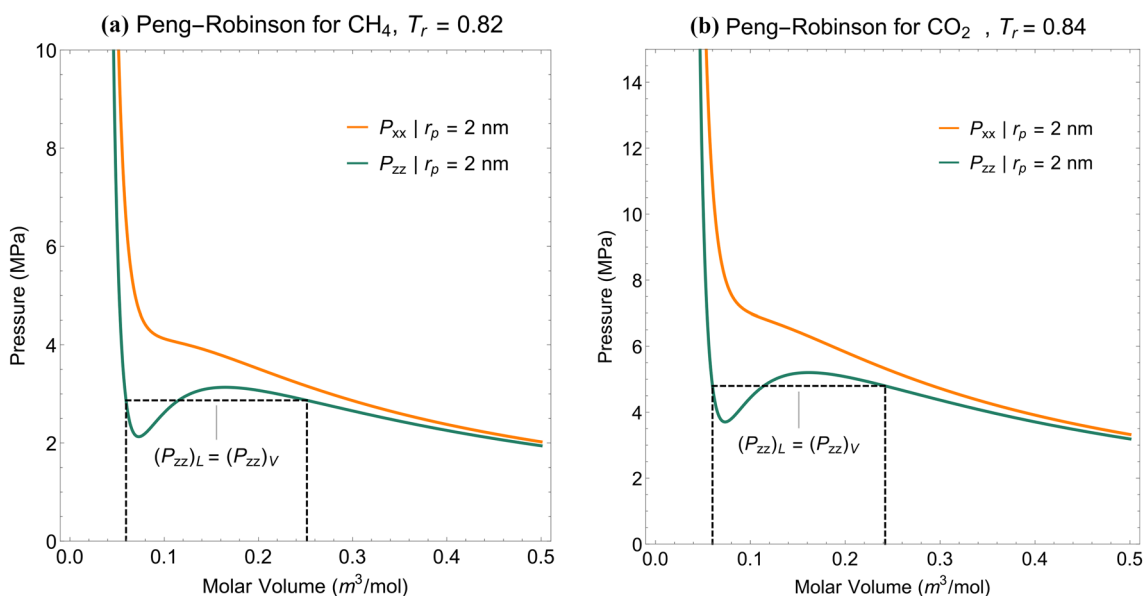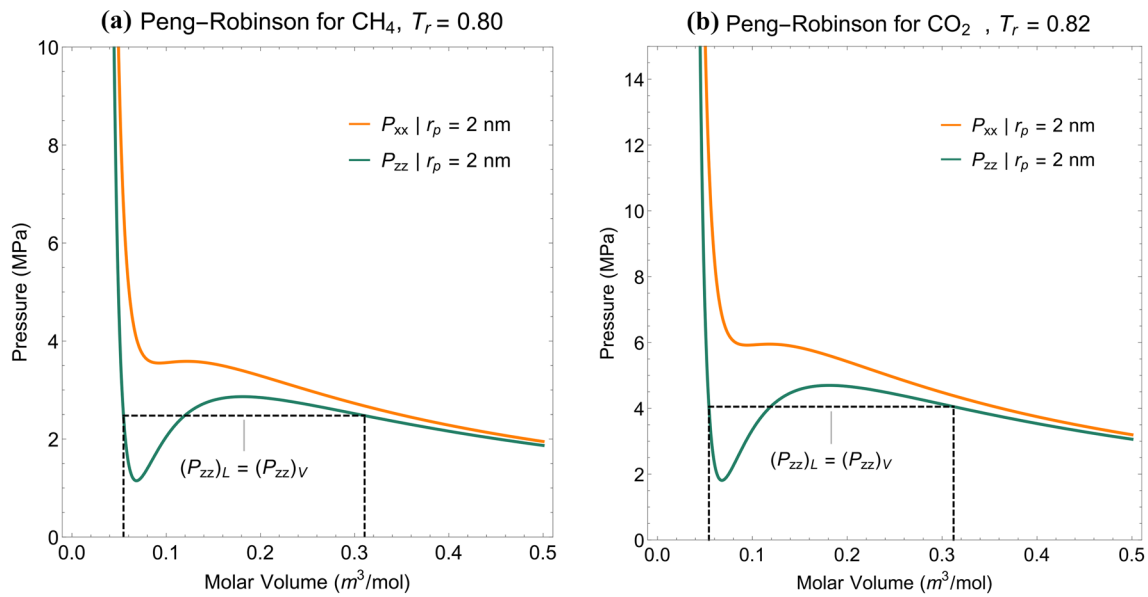

Fig. 14 Capillary condensation of Peng-Robinson for **a** methane at $T_r = 0.82$ and **b** carbon dioxide at $T_r = 0.84$ in the axial section (P_{zz})

purple colors represent the lowest and highest values of axial pressure, respectively.

Conclusions

Critical shift and phase transition of confined fluids have continually been a focal point of interest and many works have been done with the help of molecular

thermodynamics science. The model developed in this study benefits from the Kihara potential function, which has never been employed in similar studies by other researchers due to its more complex formulation and high computational cost. This potential is physically more realistic than that of previous studies, i.e., the simple Lennard–Jones potential. Our model led to a more sophisticated as well as accurate form of vdW EOS for confined matters. This, along with the new proposed adjustment

Fig. 15 Capillary condensation of Peng-Robinson for **a** methane at $T_r = 0.80$ and **b** carbon dioxide at $T_r = 0.82$ in the axial section (P_{zz}) and its tendency to act the same in the transverse one (P_{xx})

Fig. 16 P_{zz}-V-T 3D diagram of methane and carbon dioxide at $r_p = 2$ nm generated by PR-EOS
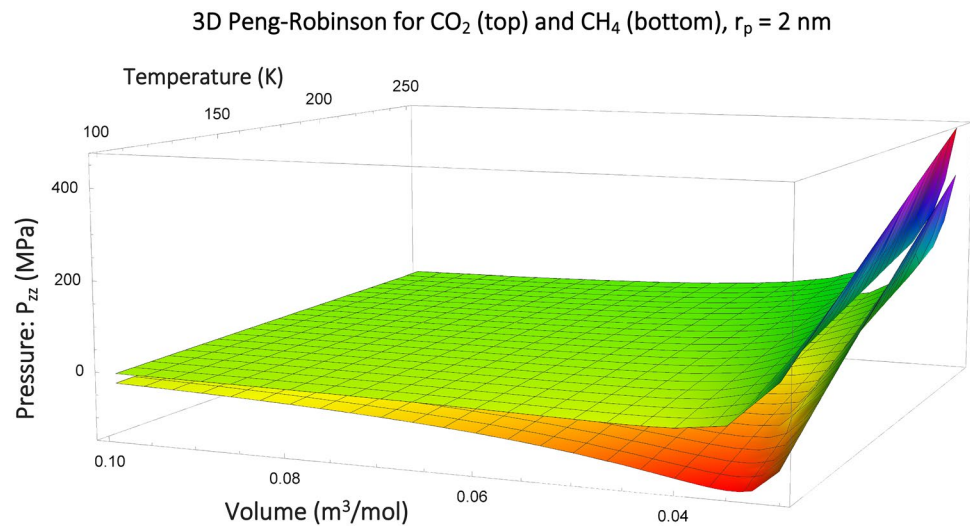
method that in contrast to previous works in the literature is thermodynamically reliable, enabled us to have more accurate predictions of critical temperature of fluids in tight porous media. The 80 datapoint used in this work is, to the best of our knowledge, the largest collection of critical shift data points ever gathered, thereby enabling us to more reliably evaluate the performance of our proposed model.

The following major conclusions can be made from this work:

- Comparing with the previous studies, the hysteresis critical temperatures (T_{ch}) of fluids were predicted with 9 percent less error in this work.
- The Kihara parameters (a_k, σ_k, and ε_k) were adjusted in order to accomplish the bulk state requirements of the developed cubic EOS. This new adjustment method was able to calculate the pore critical temperature (T_{cp}) of fluids with 6.4% less error than previous studies.
- Based on the available T_{cp} reports of some fluids, their Kihara parameters were tuned. This tuning approach had merely 0.4 percent deviation for n-alkanes.

- Regarding pressure–volume diagrams, the Kihara model demonstrated capillary condensation for both vdW and PR EOSs; however, it was reported that the L-J model does so only for the vdW EOS.

Limitations and suggestions for future works

Since the model in this study is developed particularly for calculating the shift of critical temperature of confined fluids, it is not unexpected to have erroneous predictions of critical pressure shift (P_{cp}). Hence, it is suggested to consider this issue for future works to achieve a balance between more accurate predictions of T_{cp} as well as sufficiently accurate estimations of P_{cp} by using experimental/simulation measurements, if any.

Declarations

References

Alfi M, Nasrabadi H, Banerjee D (2016) Experimental investigation of confinement effect on phase behavior of hexane, heptane and octane using lab-on-a-chip technology. Fluid Phase Equilib. https://doi.org/10.1016/j.fluid.2016.04.017

Borgnakke C, Sonntag RE (2012) Fundamentals of Thermodynamics, 8th edn. Wiley

Danesh A (1998) PVT and phase behaviour of petroleum reservoir fluids. Elsevier

Evans R, Marconi UMB, Tarazona P (1986) Capillary condensation and adsorption in cylindrical and slit-like pores. J Chem Soc Faraday Trans 2 Mol Chem Phys 10:1763–1787. https://doi.org/10.1039/F29868201763

Hansen J-P, McDonald IR (1990) Theory of simple liquids. Elsevier

Hill TL (1986) An introduction to statistical thermodynamics. Courier Corporation, North Chelmsford

Hirschfelder JO, Curtiss CF, Bird RB et al (1964) Molecular theory of gases and liquids. Wiley, New York

Islam AW, Sun AY (2017) A theory-based simple extension of Peng-Robinson equation of state for nanopore confined fluids. J Pet Explor Prod Technol 4:1197–1203. https://doi.org/10.1007/s13202-016-0306-y

Islam AW, Patzek TW, Sun AY (2015) Thermodynamics phase changes of nanopore fluids. J Nat Gas Sci Eng. https://doi.org/10.1016/j.jngse.2015.04.035

Jiang J, Sandler SI, Smit B (2004) Capillary phase transitions of n-alkanes in a carbon nanotube. Nano Lett 2:241–244. https://doi.org/10.1021/nl034961y

Jiang J, Sandler SI, Schenk M et al (2005) Adsorption and separation of linear and branched alkanes on carbon nanotube bundles from configurational-bias Monte Carlo simulation. Phys Rev B 4:045447. https://doi.org/10.1103/PhysRevB.72.045447

Jin B, Nasrabadi H (2016) Phase behavior of multi-component hydrocarbon systems in nano-pores using gauge-GCMC molecular simulation. Fluid Phase Equilib. https://doi.org/10.1016/j.fluid.2016.06.018

Jin L, Ma Y, Jamili A (2013) Investigating the effect of pore proximity on phase behavior and fluid properties in shale formations. SPE Annual Technical Conference and Exhibition. https://doi.org/10.2118/166192-MS

Johnston DC (2014) Thermodynamic properties of the van der Waals fluid. arXiv preprint arXiv:1402.1205

Kihara T (1953) Virial coefficients and models of molecules in gases. Rev Mod Phys 4:831. https://doi.org/10.1103/RevModPhys.25.831

Lowry E, Piri M (2018) Effects of chemical and physical heterogeneity on confined phase behavior in nanopores. Microporous Mesoporous Mater. https://doi.org/10.1016/j.micromeso.2017.11.045

Morishige K, Ito M (2002) Capillary condensation of nitrogen in MCM-41 and SBA-15. J Chem Phys 17:8036–8041. https://doi.org/10.1063/1.1510440

Morishige K, Shikimi M (1998) Adsorption hysteresis and pore critical temperature in a single cylindrical pore. J Chem Phys 18:7821–7824. https://doi.org/10.1063/1.476218

Morishige K, Tateishi N, Fukuma S (2003) Capillary condensation of nitrogen in MCM-48 and SBA-16. J Phys Chem B 22:5177–5181. https://doi.org/10.1021/jp022137c

Peng D-Y, Robinson DB (1976) A new two-constant equation of state. Ind Eng Chem Fundam 1:59–64. https://doi.org/10.1021/i160057a011

Peng X, Zhao J, Cao D (2007) Adsorption of carbon dioxide of 1-site and 3-site models in pillared clays: a Gibbs ensemble Monte Carlo simulation. J Colloid Interface Sci 2:391–401. https://doi.org/10.1016/j.jcis.2007.02.009

Pitakbunkate T, Balbuena PB, Moridis GJ et al (2016) Effect of confinement on pressure/volume/temperature properties of hydrocarbons in shale reservoirs. SPE J 02:621–634. https://doi.org/10.2118/170685-PA

Prausnitz JM, Lichtenthaler RN, De Azevedo EG (1998) Molecular thermodynamics of fluid-phase equilibria. Pearson Education, London

Reed TM, Gubbins KE (1973) Applied statistical mechanics. McGraw-Hill Inc, New York

Singh SK, Sinha A, Deo G et al (2009) Vapor− liquid phase coexistence, critical properties, and surface tension of confined

alkanes. J Phys Chem C 17:7170–7180. https://doi.org/10.1021/jp8073915

Smith JM, Van Ness HC, Abbott M (2005) Introduction to Chemical Engineering Thermodynamics. McGraw-Hill Education, New York

Song Z, Song Y, Guo J et al (2020) Adsorption induced critical shifts of confined fluids in shale nanopores. Chem Eng J. https://doi.org/10.1016/j.cej.2019.123837

Tan SJ, Prasetyo L, Zeng Y et al (2017) On the consistency of NVT, NPT, µVT and Gibbs ensembles in the framework of kinetic Monte Carlo-Fluid phase equilibria and adsorption of pure component systems. Chem Eng J. https://doi.org/10.1016/j.cej.2017.01.079

Tan SP, Qiu X, Dejam M et al (2019) Critical point of fluid confined in nanopores: experimental detection and measurement. J Phys Chem C 15:9824–9830. https://doi.org/10.1021/acs.jpcc.9b00299

Tee LS, Gotoh S, Stewart WE (1966a) Molecular parameters for normal fluids. Kihara potential with spherical core. Ind Eng Chem Fundam 3:363–367. https://doi.org/10.1021/i160019a012

Tee LS, Gotoh S, Stewart WE (1966b) Molecular parameters for normal fluids. Lennard-Jones 12–6 potential. Ind Eng Chem Fundam 3:356–363. https://doi.org/10.1021/i160019a011

Wang P, Huang S, Zhao F et al (2021) Modeling phase behavior of nano-confined fluids in shale reservoirs with a modified Soave-Redlich-Kwong equation of state. Chem Eng J. https://doi.org/10.1016/j.cej.2021.133661

Wong K, Zeng Q, Yu A (2009) Gold catalysts: a new insight into the molecular adsorption and CO oxidation. Chem Eng J 3:824–828. https://doi.org/10.1016/j.cej.2009.09.006

Yang G, Li X (2020) Modified Peng-Robinson equation of state for CO2/hydrocarbon systems within nanopores. J Nat Gas Sci Eng. https://doi.org/10.1016/j.jngse.2020.103700

Yang G, Fan Z, Li X (2019) Determination of confined fluid phase behavior using extended Peng-Robinson equation of state. Chem Eng J. https://doi.org/10.1016/j.cej.2019.122032

Zarragoicoechea GJ, Kuz VA (2002) van der Waals equation of state for a fluid in a nanopore. Phys Rev E 65(2):021110. https://doi.org/10.1103/PhysRevE.65.021110

Zarragoicoechea GJ, Kuz VA (2004) Critical shift of a confined fluid in a nanopore. Fluid Phase Equilib 1:7–9. https://doi.org/10.1103/PhysRevE.65.021110

Zhang K, Jia N, Li S et al (2018a) Millimeter to nanometer-scale tight oil–CO2 solubility parameter and minimum miscibility pressure calculations. Fuel. https://doi.org/10.1016/j.fuel.2018.02.032

Zhang K, Jia N, Li S et al (2018b) Thermodynamic phase behaviour and miscibility of confined fluids in nanopores. Chem Eng J 351:1115–1128

Zhang K, Jia N, Liu L (2018c) Adsorption thicknesses of confined pure and mixing fluids in nanopores. Langmuir 43:12815–12826. https://doi.org/10.1021/acs.langmuir.8b02925

Zhang K, Jia N, Liu L (2019a) Generalized critical shifts of confined fluids in nanopores with adsorptions. Chem Eng J. https://doi.org/10.1016/j.cej.2019.04.198

Zhang K, Jia N, Liu L (2019b) Nanoscale-extended alpha functions for pure and mixing confined fluids. Fluid Phase Equilib. https://doi.org/10.1016/j.fluid.2018.10.018